nature nanotechnology

Article

https://doi.org/10.1038/s41565-024-01620-6

Chimeric nanobody-decorated liposomes by self-assembly

Received: 5 May 2023

Accepted: 23 January 2024

Published online: 19 February 2024



Md. Mofizur Rahman $\textcircled{0}^{1,2;18}$, Jing Wang $\textcircled{0}^{3,4;18}$, Guosheng Wang $\textcircled{0}^{1,5;18}$, Zhipeng Su 6 , Yizeng Li $\textcircled{0}^{7}$, Yundi Chen 1 , Jinguo Meng 6 , Yao Yao 6 , Lefei Wang 6 , Stephan Wilkens 8 , Jifu Tan $\textcircled{0}^9$, Juntao Luo $\textcircled{0}^{10}$, Tao Zhang $\textcircled{0}^{11}$, Chuandong Zhu 1,12 , Sung Hyun Cho $\textcircled{0}^{13}$, Lixue Wang $\textcircled{0}^{1,12} \bowtie$, Luke P. Lee $\textcircled{0}^{14,15;16;17} \bowtie$ & Yuan Wan $\textcircled{0}^{1} \bowtie$

Liposomes as drug vehicles have advantages, such as payload protection, tunable carrying capacity and improved biodistribution. However, due to the dysfunction of targeting moieties and payload loss during preparation, immunoliposomes have yet to be favoured in commercial manufacturing. Here we report a chemical modification-free biophysical approach for producing immunoliposomes in one step through the self-assembly of a chimeric nanobody (cNB) into liposome bilayers. cNB consists of a nanobody against human epidermal growth factor receptor 2 (HER2), a flexible peptide linker and a hydrophobic single transmembrane domain. We determined that 64% of therapeutic compounds can be encapsulated into 100-nm liposomes, and up to 2,500 cNBs can be anchored on liposomal membranes without steric hindrance under facile conditions. Subsequently, we demonstrate that drug-loaded immunoliposomes increase cytotoxicity on HER2-overexpressing cancer cell lines by 10- to 20-fold, inhibit the growth of xenograft tumours by 3.4-fold and improve survival by more than twofold.

Immunoliposomes, featuring a large payload capacity, altered pharmacokinetics, improved drug tolerance and enhanced lesion-specific distribution^{1–5}, encounter challenges in industrial translation due, in part, to the absence of cost-effective, scalable manufacturing technology^{6,7}. The existing preparation procedure involves laborious chemical modification, compromising the stability of targeting moieties.

Payload leakage and product loss are also inevitable during the lengthy production process. Despite current efforts $^{8-11}$, these challenges persist, and immunoliposomes remain unappealing to manufacturers due to the high production cost and batch-to-batch variation. Moreover, selecting full-length antibodies, antibody fragments or aptamers as targeting moieties poses challenges in size, biocompatibility and stability,

¹The Pq Laboratory of BiomeDx/Rx, Department of Biomedical Engineering, Binghamton University, Binghamton, NY, USA. ²Department of Pharmacy, Daffodil International University, Dhaka, Bangladesh. ³Department of Hematology, Nanjing Drum Tower Hospital, Affiliated Hospital of Medical School, Nanjing University, Nanjing, China. ⁴Department of Oncology and Hematology, Yizheng Hospital of Nanjing Drum Tower Hospital Group, Yizheng, China. ⁵Department of Pulmonary and Critical Care Medicine, Shanghai East Hospital, Tongji University School of Medicine, Shanghai, China. ⁶Nanjing Regenecore Biotech Co. Ltd., Nanjing, China. ⁷Biophysics and Mathematical Biology Lab, Department of Biomedical Engineering, Binghamton University, Binghamton, NY, USA. ⁸Department of Biochemistry and Molecular Biology, Upstate Medical University, Syracuse, NY, USA. ⁹Department of Mechanical Engineering, Northern Illinois University, Dekalb, IL, USA. ¹⁰Department of Pharmacology, Upstate Medical University, Syracuse, NY, USA. ¹¹School of Pharmacy and Pharmaceutical Sciences, Binghamton University, Johnson City, NY, USA. ¹²Department of Radiotherapy, The Second Hospital of Nanjing, Nanjing University of Chinese Medicine, Nanjing, China. ¹³Huck Institutes of the Life Sciences, The Pennsylvania State University, University Park, PA, USA. ¹⁴Harvard Medical School, Harvard University; Department of Medicine, Brigham and Women's Hospital, Boston, MA, USA. ¹⁵Department of Bioengineering, Department of Electrical Engineering and Computer Science, University of California, Berkeley, CA, USA. ¹⁶Department of Biophysics, Institute of Quantum Biophysics, Sungkyunkwan University, Suwon, Korea. ¹⁷Department of Chemistry and Nanoscience, Ewha Womans University, Seoul, Korea. ¹⁸These authors contributed equally: Md. Mofizur Rahman, Jing Wang, Guosheng Wang. —e-mail: lixue.wang@njucm.edu.cn; lplee@bwh.harvard.edu; ywan@binghamton.edu

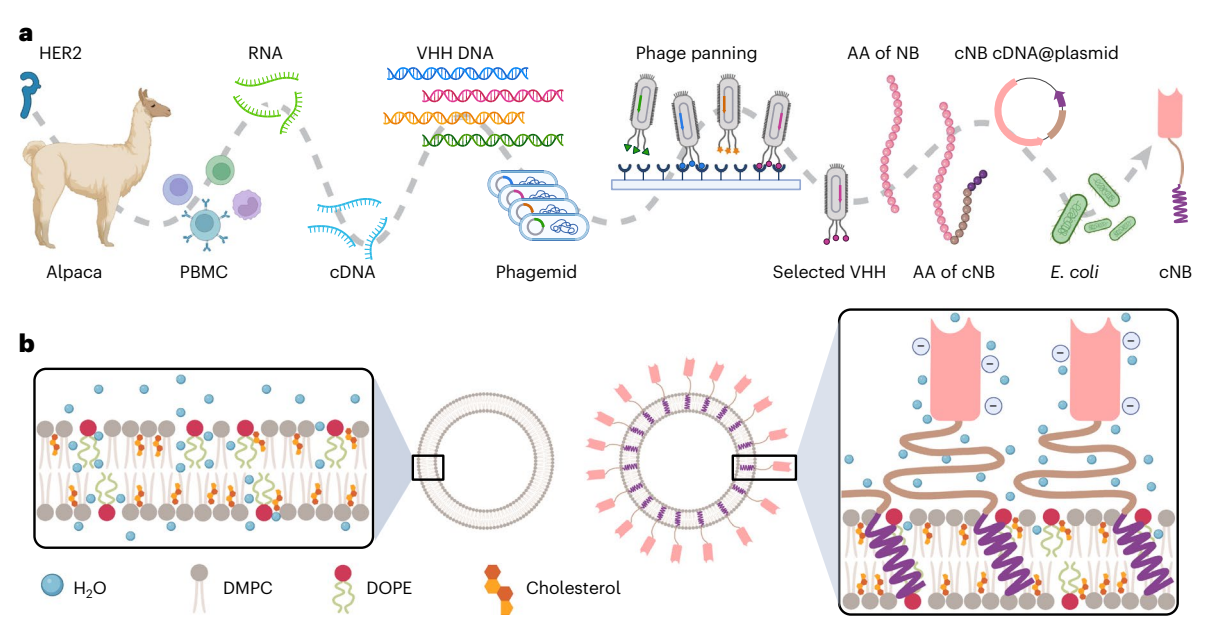


Fig. 1| **Schematic of immunoliposome preparation. a**, Flowchart illustrating the manufacturing processes of cNB. Alpacas were immunized with the HER2 extracellular domain, and subsequent isolation of peripheral blood mononuclear cells (PBMCs) was performed. Total RNA was extracted from the PBMCs followed by cDNA synthesis for amplifying variable heavy domain of heavy chain (VHH) gene regions. The PCR products were then ligated into the phagemid vector, and *E. coli* cells were transformed with the ligated products and cultured. Colonies were recovered for the biopanning of phage displayed VHH libraries. One

specific VHH was selected and sequenced to determine its amino acid sequences. Subsequently, in the design process amino acids encoding a hydrophilic linker (shown in yellow) and a STMD (shown in purple) were added to the C-terminus of the NB. The corresponding cDNA was synthesized and integrated into plasmids for the expression of the cNB using *E. coli* cells. **b**, Overview of biophysical transformation due to size, surface charge, lipid fluidity, membrane stiffness and thermostability between liposome and cNB-LP. AA, amino acid.

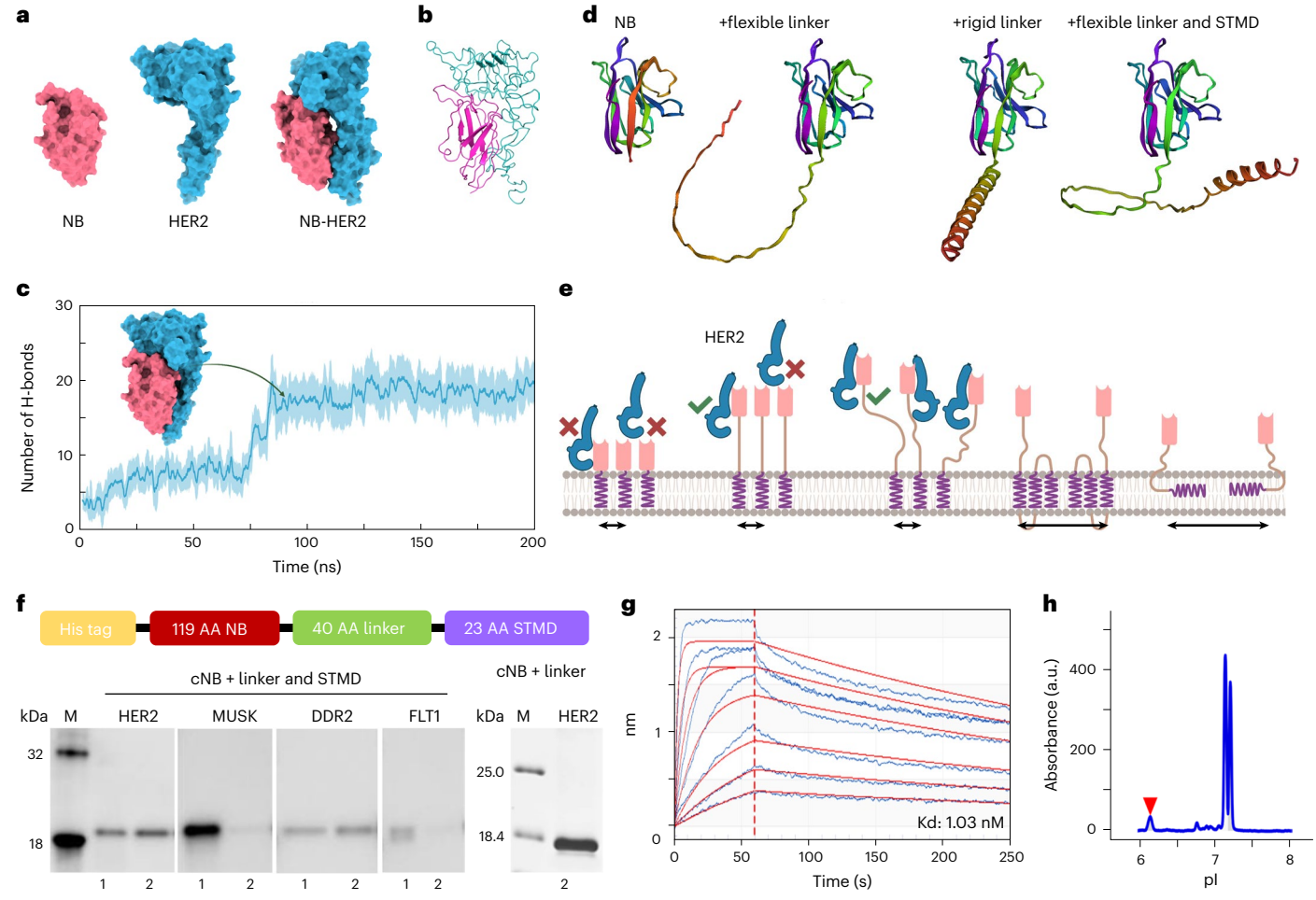
compromising immunoliposomal performance 12-14. Contrastingly, small-sized, low-immunogenic and stable nanobodies (NB) are suitable as targeting moieties 15. Here, we report a strategy for preparing immunoliposomes in one step. Briefly, chimeric nanobodies (cNB), produced in bacteria (Fig. 1a), consist of a NB against human epidermal growth factor receptor 2 (HER2), a flexible peptide linker and a human single transmembrane domain (STMD). The lipids, drugs and cNBs in an optimized ratio self-assemble into immunoliposomes. The integration of cNBs can alter biophysical properties of liposomes (Fig. 1b). Altogether, our method enables immunoliposomal production using the existing manufacturing pipeline, showing promise for industrial manufacturing and clinical use.

NB and cNB

Screening 282 colonies, we identified 39 NBs specifically binding to HER2. One NB with K_d of 0.53 nM was selected for production, and Escherichia coli was preferred over CHO cells for its cost-effectiveness (Supplementary Fig. 1a,b). The EC₅₀ (half maximal effective concentration) of collected NB was 0.54 nM (Supplementary Fig. 1c). Antibody-dependent cellular cytotoxicity was not observed due to the absence of an Fc domain (Supplementary Fig. 1d). The NB did inhibit HER2-overexpressing SK-BR-3 cells (Supplementary Fig. 1e), indicating the NB solely has a targeting effect. Moreover, the NB is negatively charged at physiological pH (Supplementary Fig. 1f). The NB/HER2 complex is stabilized by complementary structure, hydrogen bonds and electrostatic interactions. The NB primarily binds to domains IV and II of HER2 (Supplementary Fig. 2). The complex achieved equilibrium, with the minimal root mean square fluctuation values being less than 0.1 nm (Supplementary Fig. 3a,b). Only three regions displayed a relatively large root mean square fluctuation of ~0.2 nm. These regions located outside the main interaction surface and thus would not weaken the overall equilibrium. The complex is stabilized by ~17 H-bonds and a complementary electrostatic potential surface between NB and HER2 (Fig. 2c and Supplementary Fig. 4a,b). The average binding free energy of the NB/HER2 complex was -90.12 kcal mol $^{-1}$ (Supplementary Fig. 5a). The $G_{\rm gas}$ and $G_{\rm solv}$ were -838.05 and 747.94 kcal mol $^{-1}$, respectively (Supplementary Fig. 5b). Several amino acid residuals of HER2 and NB primarily engage in the interaction (Supplementary Fig. 5c,d). Beneficial mutations may further enhance the binding affinity.

We designed the cNB and predicted its 3D structure (Fig. 2d and Supplementary Fig. 6). A flexible (GGGGS)₈ linker and a rigid (EAAAK)₈ linker were investigated. The (GGGGS)_o fold-breaking linker enhances the mobility, reduces steric hindrance and improves bioactivity of the NB¹⁶. Meanwhile, the (GGGGS)₈ linker maintains stability in aqueous solutions, which reduces the unfavourable interaction between the linker and the NB. In contrast, the (EAAAK)₈ linker exhibits stiff structures, ensuring a fixed distance between the NB and the liposomal membranes. However, the limited movement of the NB may impact the NB/HER2 interaction (Fig. 2e). The hydrophobic (EAAAK)₈ linker with an auto-cleavage feature may also lead to the loss of the NB, compromising targeted delivery. We did not consider multi-pass transmembrane proteins, monotopic membrane proteins or β-sheet peptides. These transmembrane proteins occupy ample space, lowering their grafting density (Fig. 2e). Altogether, the cNB with a (GGGGS)₈ linker of ~20 nm length was designed 16. The decoration of the cNBs on liposomal membranes could form a protein sheath layer with a thickness of at least ~6 nm. The hydrophilic and anionic sheath layer could prevent fouling and reduce phagocytic clearance.

We further added a His6 tag to the N-terminus and a STMD to the C-terminus (Fig. 2f). Four human STMDs were compared (Supplementary Fig. 7a) 17 . MUSK, HER2 and DDR2 are neutral, gradually increasing in hydrophobicity. MUSK and FLT1 have similar hydrophobicity, but FLT1 is negatively charged. Artificial peptides were excluded, known to induce membrane disruption 18 . The produced cNBs can be collected from the supernatant of cell lysate (Fig. 2f), with abundant cNBs found in the pellet (Supplementary Fig. 7b). The expression level of four cNBs



 $\label{eq:Fig.2} \textbf{PCA} (\textbf{Characterization of NB and engineered cNB. a}, \textbf{Structural model of identified anti-HER2 NB, HER2 and the NB/HER2 complex. b}, \textbf{Crystal structure of NB/HER2 complex. c}, \textbf{Prediction of formed hydrogen bonds in NB/HER2 complex throughout 200 ns of molecular dynamics simulation (mean value <math>\pm$ s.d. shown). d, \textbf{Crystal structure of NB, cNB that harbours only a flexible linker, cNB that harbours only a rigid linker, and cNB that harbours a flexible linker and the structure of NB constants and the structure of NB constants are structured in the structure of NB constants and the structure of NB constants are structured in the structured in the structure of NB constants are structured in the struc

STMD. **e**, Illustration of potential steric hindrance effect and cNB grafting density influenced different linkers or transmembrane domains. **f**, Designed amino acid (AA) sequence of cNB (top) and western blot of cNB with various STMD (bottom) prepared at $15\,^{\circ}$ C for $16\,h$ (1) and at $37\,^{\circ}$ C for $4\,h$ (2). Experiments were repeated five times. **g**, Kinetic analysis of cNB at pH 7.4. **h**, Isoelectric point analysis of cNB. Experiments were repeated five times.

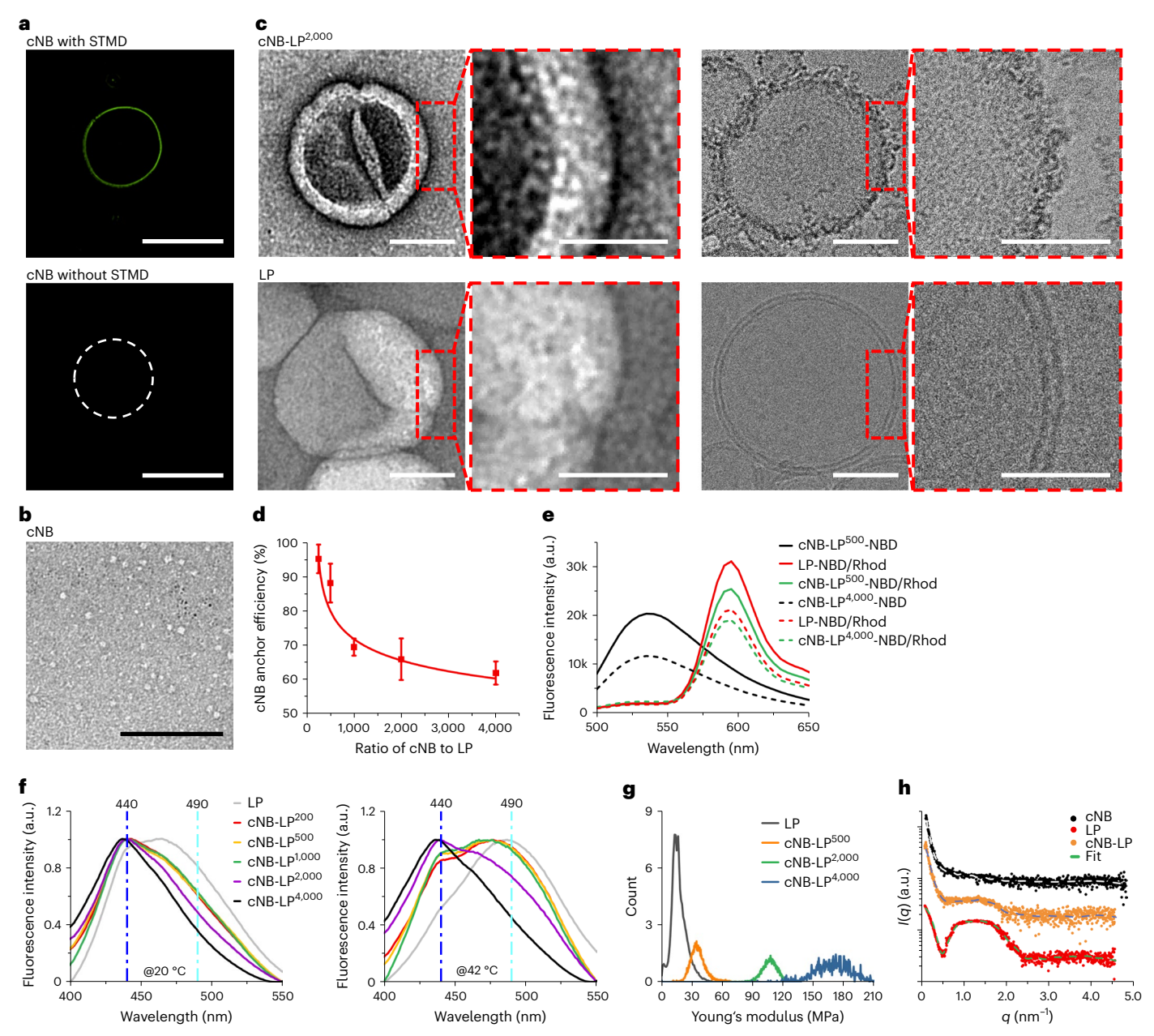
was similar, suggesting that the hydrophobicity and surface charge of STMD do not significantly influence cNB production. Indeed, STMD lowered the yield and solubility of cNB compared with the counterpart with only the (GGGGS)₈ linker (Supplementary Fig. 7b). Among the four variants, the HER2-harbouring cNB showed a reliable yield, and thus we collected this cNB with a purity of 98% for the subsequent studies (Supplementary Fig. 7c,d). The K_d and the pl of cNB did not significantly alter due to the adoption of the neural linker and STMD (Fig. 2g,h).

cNB-decorated liposomes

cNB-decorated liposomes (cNB-LPs) were prepared, and the anchored cNBs were observed with anti-His6 fluorescent antibodies (Fig. 3a). Transmission electron microscopy (TEM) visualized 100-nm plain LPs and cNB-LP prepared in two cNB-to-LP ratios, that is, 200:1 (cNB-LP²⁰⁰) and 2,000:1 (cNB-LP^{2,000}) (Supplementary Fig. 8). cNB clusters formed during sample dehydration and appeared as white dots with a diameter less than 8 nm (Fig. 3b). A coarse edge was observed in cNB-LPs as opposed to LPs (Fig. 3c). The membrane thickness of LPs was ~4 nm, which increased to ~10 nm in cNB-LPs. We ruled out the formation of cNB micelles. Computational results showed that these cNBs were not arranged in a head-to-head and tail-to-tail manner (Supplementary Fig. 9a). The low binding energy between cNBs revealed that the aggregation

was highly unstable (Supplementary Fig. 9b,c). The circular dichroism spectra of cNB and cNB-LP^{2,000} exhibited the characteristic profile of an α -helix configuration (Supplementary Fig. 9d), but not a robust helix-helix structure. The intensity ratio of 222/208 for cNB and cNB-LP^{2,000} was only 0.80 and 0.85, respectively, indicating dispersed helical structures 19 . Moreover, if cNB micelles were present, their diameter would probably measure ~25 nm or more, inconsistent with TEM and size analysis (Supplementary Fig. 9e,f).

The fluorescence resonance energy transfer (FRET) assay also verified cNB integration into liposomal membranes (Supplementary Fig. 10a). Moreover, the fluorescence characteristics of cNB-LP^{1,000}, compared with cNB-LP⁵⁰⁰, revealed more efficient energy transfer. The difference was attributed to increased cNB density and decreased inter-cNB distance on membranes. The anchor efficiency of cNB decreased from 95.3% to 61.9% when the mixing ratio of cNB to LP increased from 200 to 4,000 (Fig. 3d and Supplementary Fig. 10b). Equivalently, -190 to -2,500 cNBs were integrated to 100-nm LPs. In contrast, a limited number of NBs can be grafted on LPs using conventional methods²⁰⁻²⁵. One study reported the optimal number of NBs for achieving ideal targeting specificity and efficiency²⁶. The findings may not be applicable to our cNB-LPs due to the use of PEG and variations in liposomal size. Nevertheless, a few hundred cNBs are sufficient for targeted drug delivery²⁰, and our method can readily adjust the number



 $\label{eq:continuous} \textbf{Fig. 3} \ | \ \textbf{Characterization of biophysical properties of cNB-LPs.} \\ \textbf{a}, \\ \text{Immunofluorescence staining of a LP decorated with cNBs (top) and STMD-deficient cNBs (bottom). Scale bar, 5 <math>\mu$ m. Experiments were repeated five times. \textbf{b}, TEM image shows the morphology of cNBs. Scale bar, 100 nm. Experiments were repeated three times. \textbf{c}, The cryo-TEM (left) and TEM (right) images show the membrane morphology of a typical cNB-LP².000 and a typical plain LP. Scale bar, 50 nm. Experiments were repeated three times. \textbf{d}, Decoration efficiency of the continuous co

cNB as a function of cNB quantity (n=12, mean value \pm s.d.). **e**, Fluorescence signals of FRET-pair labelled cNB-LPs and LPs. **f**, The fluorescence signals of Laurdan emission from various cNB-LP at 20 °C and 42 °C. **g**, Stiffness distribution for free LPs and cNB-LPs (n=100 in LP group; n=87 in cNB-LP⁵⁰⁰ group; n=51 in cNB-LP^{2,000} group; n=34 in cNBLP^{4,000} group). **h**, SAXS scattering curves measured for plain LP, free cNB, and cNB-LP^{2,000} samples in solution.

of cNBs. We speculated that cNBs anchor onto both outer and inner membranes. The interval between two nearby cNBs in cNB-LP 200 is ~10 nm if 190 cNBs fully incorporate into the outer membranes, and FRET occurs within this proximity 27 . However, no fluorescence change was observed, indicating that adjacent cNBs were over 10 nm apart. A few cNBs might anchor on the inner membranes. Given the outer and inner surface areas of LPs are nearly identical, we presumed homogeneous anchoring of cNBs on two sides. Thus, for cNB-LP 200 , cNB-LP 500 and cNB-LP 1,000 , ~95, ~220 and ~345 cNBs were on the outer membranes, resulting in intervals of ~18.2, ~9.3 and ~4.2 nm, respectively. The FRET data supported this calculation. We also deduced that cNBs were homogeneously distributed over the membranes rather than anchored as

blocks (Fig. 3e and Supplementary Fig. 10c), as evidenced by almost identical FRET efficiencies of cNB-LPs and LPs at 535 nm. The quantity of cNB did not impact its homogeneous distribution.

Membrane fluidity was studied with a Laurdan assay (Fig. 3f and Supplementary Fig. 11a) 28 . The fluid and gel phase lead to emission at 490 and 440 nm, respectively. At 20 °C, cNB-LPs showed low membrane fluidity compared with the plain LPs. At 42 °C, the emission peak of LPs was detected at 490 nm. The emissions of cNB-LP 200 , cNB-LP 500 and cNB-LP 1,000 shifted towards 490 nm. Only cNB-LP 2,000 and cNB-LP 4,000 kept the emission peak at 440 nm. In brief, the membrane fluidity of cNB-LPs and plain LPs increased with temperature (Supplementary Fig. 11b). The higher the number of anchored cNBs, the lower the

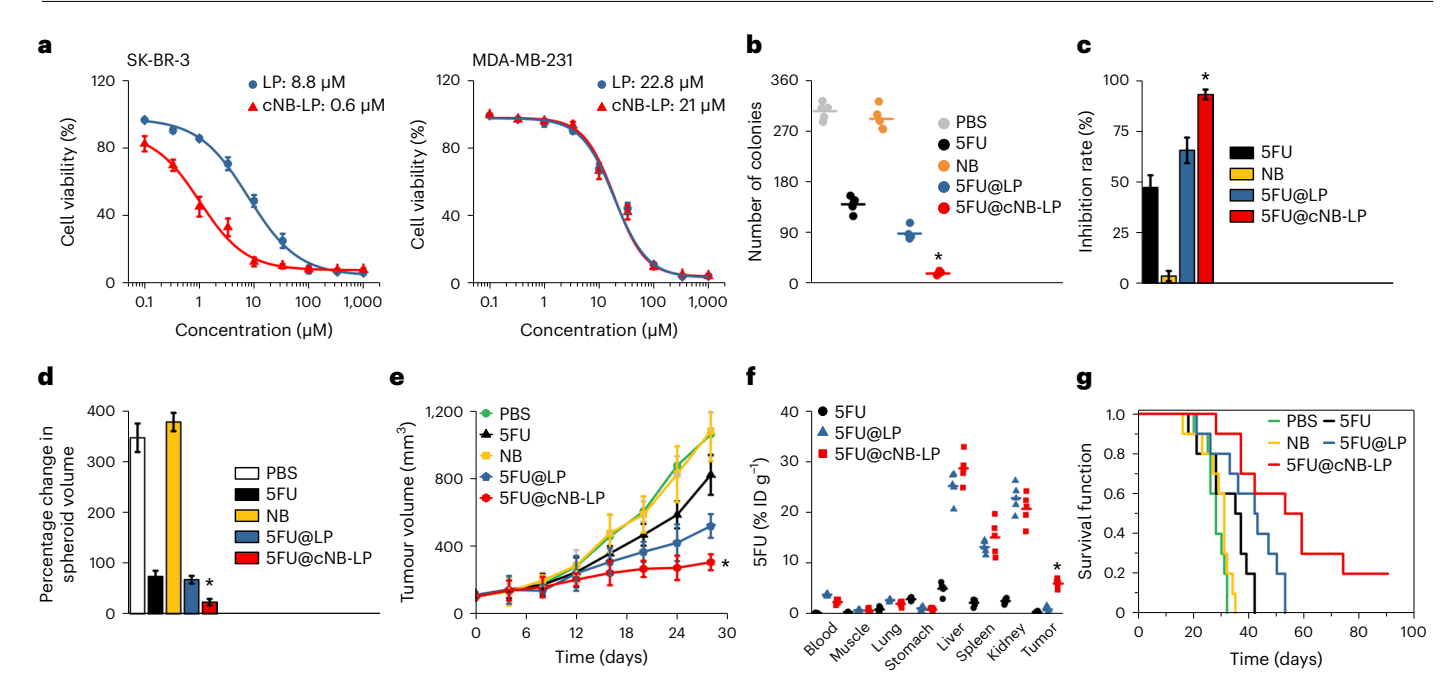


Fig. 4 | **Tumour treatment in vitro and in vivo. a**, Respective IC_{50} values of SFU-loaded LPs and SFU-loaded cNB-LPs in treatment of MDA-MB-231 cells and SK-BR-3 cells (n=12, mean value \pm s.d.). **b**, Growth inhibition on SK-BR-3 colonies in the respective group (n=5, mean values shown; P<0.001, one-way ANOVA). **c**, Inhibition of migration of SK-BR-3 cells in the respective group (n=12, mean value \pm s.d.; P<0.001, one-way ANOVA). **d**, Volume changes in the SK-BR-3 spheroids in the respective group (n=20, mean value \pm s.d.; P<0.001, one-way

decline rate of polarization and the more stable the cNB-LPs. In addi-

ANOVA). **e**, Tumour volume of SK-BR-3 orthotopic tumour xenograft in mice after drug or placebo administration. **f**, Biodistribution of 5FU in major organs at 24 h post-administration. Five biological replicates were measured (n = 5, mean values were shown; P < 0.001, one-way ANOVA). **g**, Survival curves for mice bearing SK-BR-3 orthotopic tumour after drug or placebo administration (ten mice in each group).

tion, crystalline melting curves suggested that incorporating cNBs improved the thermostability of cNB-LPs (Supplementary Fig. 11c). In controls, cNBs exhibited no noticeable phase transition, while the LPs displayed a melting temperature of ~24 °C as expected. We further examined this finding with a computational model (Supplementary Fig. 12a-f). cNBs can enhance the membrane stiffness when $\frac{k_n}{n} > 0.89$, where k_n is the interaction between an STMD and a lipid, and k_n is the interaction between two adjacent lipids (Supplementary Fig. 12g). The condition requires STMD-lipid interaction strength to be nearly equivalent to lipid-lipid interaction. Due to unknown value of k_n and k_n , we calculated $\frac{k_n}{k_n}$ using the intermolecular distance and bonding energy (Supplementary Fig. 12h). The $\Delta G_{\text{transfer}}$ of STMD-lipid and lipid-lipid is -28.8 and -6 kcal mol⁻¹, respectively^{29,30}. Using G to approximate minimum bonding energy, we obtained $\frac{E_{0,n}}{E_{0,p}} \approx 5$. Therefore, more cNBs could increase the membrane stiffness (Supplementary Fig. 12g). The finding was verified by measurements of rigidity in plain LPs and cNB-LPs. The Young's modulus values for plain LPs, cNB-LP⁵⁰⁰, cNB-LP^{2,000} and cNB-LP^{4,000} were 14.9, 34.4, 107.7 and 174.3 MPa, respec-

The ζ -potential of free cNBs increased as the pH value decreased (Supplementary Fig. 14a). The ζ -potential of cNB-LPs at pH 7.4 significantly decreased with increasing anchored cNBs. We observed the opposite phenomenon at pH 5.5 (Supplementary Fig. 14b). In the acidic tumour microenvironment, positively charged cNB-LPs may facilitate the NB-HER2 binding. In parallel, we demonstrated that cNB-LPs can bind to native HER2 on cell membranes (Supplementary Fig. 15). A computational model revealed that more cNBs on membranes increase the adhesion probability of cNB-LPs under the same shear rate (Supplementary Fig. 16)³¹. In small-angle X-ray scattering (SAXS),

tively (Fig. 3g and Supplementary Fig. 13). The stiffness distribution

curves illustrated that as the number of cNBs increased, rigidity pro-

portionally escalated.

cNB-LP^{2,000} exhibited a distinct change in patterns compared with LPs and cNBs, suggesting the integration of cNBs into the lipid membranes (Fig. 3h). SAXS detected an average size of 4.71 nm for cNBs, the average bilayer thickness of plain LPs was 35.97 Å, and the cNB shell had an average thickness of 56.43 Å. These values agreed with the cryogenic (cryo)-TEM measurements. Moreover, no distinct peak was evident in the low q region, indicating that cNBs did not form micelles 32 .

Summarizing our findings, we selected cNB-LP^{2,000} for subsequent studies. The average size of fresh cNB-LP^{2,000} was 117.7 nm, and the size of cryopreserved ones increased to 142.7 nm over 60 days (Supplementary Fig. 17a–c). No significant size differences were observed in cNB-LP^{2,000} stored at 4 °C for over 10 months, and pH had no significant effect on size of cNB-LP^{2,000} during a 30-h period at 37 °C (Supplementary Fig. 17d,e). These findings demonstrated the stability of cNB-LP^{2,000}.

Treatment efficacy

5-Fluorouracil (5FU) was used. The loading efficiency increased with the lipid-to-5FU ratio, reaching a maximum of ~75% at a ratio of 20 (Supplementary Fig. 18a). No significant difference in loading efficiency was identified between LPs and cNB-LP^{2,000}. We selected a ratio of 5, achieving loading efficiency of 64.9% in cNB-LP^{2,000}. After a 14-h incubation at 37 °C, over 95% of the loaded 5FU was released from LPs (Supplementary Fig. 18b). In contrast, cNB-LP^{2,000} released -46% and -50% after 30 h at pH 7.4 and pH 5.5, respectively. Moreover, ~94% of the initially encapsulated 5FU remained within the core of LPs and cNB-LP^{2,000} after 30 h at 4 °C, and ~86% was retained after 10-month storage at 4 °C. In addition, the loading efficiency of dextran-3k and dextran-10k in cNB-LP^{2,000} averaged 21.5% and 28.6%, respectively, matching reported values obtained with LPs³³⁻³⁵. At 37 °C, LPs released over 95% of wrapped dextran after 26-h incubation, but retained them well at 4 °C. Conversely, dextran were preserved in cNB-LP^{2,000}, and elevated temperature induced slightly more release (Supplementary Fig. 18c,d).

Next, we tested HER2-overexpression cell lines and counterparts (Supplementary Fig. 19a). The IC₅₀ (half maximal inhibitory concentration) of 5FU-loaded cNB-LP^{2,000} in treating SK-BR-3 cells was 0.6 μM, compared with 8.8 µM for 5FU-loaded LPs (Fig. 4a), demonstrating a 14.7-fold enhancement. In the treatment of MDA-MB-231 cells, the IC₅₀ of two groups showed no significant change. Similar results were observed in eight other cell lines (Supplementary Fig. 19b). Treatment efficacy improved by 3.3- to 13.6-fold, depending on the HER2 level and sensitivity to 5FU in respective cell line. Additional cell assays demonstrated that cNB-LP^{2,000} improved treatment efficacy in comparison with controls. The inhibitory efficacy of cNB-LP^{2,000} in colony formation was 8.2- and 5.2-fold higher than that of free 5FU and 5FU-loaded LPs (Fig. 4b). The inhibition rate of cNB-LP^{2,000} in cell invasion was 2- and 1.4-fold higher than that of two controls (Fig. 4c). The volume of SK-BR-3 spheroid in cNB-LP^{2,000} and LP groups decreased 14.3- and 5.1-fold (Fig. 4d and Supplementary Fig. 19c), compared with that in two negative controls.

Free NBs did not show treatment efficacy or systemic toxicity in animal studies. There was no significant difference in blood tests between phosphate-buffered saline (PBS) and NB groups (Supplementary Fig. 20a). In SK-BR-3 orthotopic model, the tumour volume in cNB-LP^{2,000} group was 3.5- and 1.7-fold smaller than that of PBS and LP groups (Fig. 4e and Supplementary Fig. 20b). The tumour weight in cNB-LP $^{\!2,000}$ and LP groups was 8.6- and 4.6-fold lighter than that of PBS control (Supplementary Fig. 20c). Tumour tissue damage and reduced Ki67 index were observed in the cNB-LP^{2,000} group compared with others (Supplementary Fig. 20d). Body weight showed no significant difference (Supplementary Fig. 20e). Extensive damage in major organs was not observed in any groups (Supplementary Fig. 21). But histological changes were identified in the liver and spleen due to the uptake of cNB-LP^{2,000} and LPs. Next, we investigated the biodistribution of 5FU in vivo. In cNB-LP^{2,000} group, 5FU concentration in tumours was 18.7- and 6.9-fold higher than that in free 5FU and LP groups at 24 h post-administration (Fig. 4f). 5FU-loaded cNB-LP^{2,000} significantly improved the median survival time of SK-BR-3 tumour-bearing mice from 28 to 56 days (Fig. 4g). Additionally, an NCI-N87 subcutaneous model was investigated. The tumour volume of NCI-N87 was 10.4-, 5.6- and 1.6-fold smaller than that of the PBS, free 5FU and LP groups, respectively (Supplementary Fig. 22).

Conclusions

We used a typical composition of PC/PE/cholesterol to mimic mammalian cell membranes while ensuring stability under physiological conditions³⁶. cNB-LPs may prefer lipids with low melting temperature (T_m) . Optimal fluidity of the liposomal membrane may promote the incorporation of STMD. For example, 1,2-Dimyristoyl-sn-glycero-3-p hosphocholine (DMPC) has excellent miscibility and interactions with STMD^{19,37}, leading to the formation of highly stable cNB-LPs in this study. In contrast, high- T_m lipids may not interact favourably with STMD, risking the stability of membrane-anchoring cNBs³⁸. Alternatively, this combination may result in highly stiff cNB-LPs with limited loading capacity and high immunogenicity. Moreover, we reduced the percentage of 1,2-dioleoyl-sn-glycero-3-phosphoethanolamine (DOPE) to 20%. This modification did not induce destabilization of plain LPs or cNB-LPs, but still can promote membrane fusion and cytosolic delivery³⁹⁻⁴². Furthermore, we lowered the cholesterol content to 10%. High cholesterol content results in the formation of highly ordered lipid phase and membrane protein segregation⁴³, potentially limiting the incorporation of cNBs. Hence, we used a minimal cholesterol concentration, allowing cholesterol and STMD to jointly occupy the vacant spaces within the liposomal acyl chain, co-contributing to the stabilization of cNB-LPs. Generally, our cNB-LPs exhibit enhanced membrane stiffness, imperviousness. The insertion of STMD does not significantly rearrange the surrounding lipids44,45. On the contrary, the integration of STMD may enforce tight packing of DMPC/DOPE^{46,47}, limit their lateral movement,

and thus increase membrane stiffness and stability. Rigid NBs with substantial heat capacity may further enhance these changes. In addition to lipids, the linker and hypoallergenic STMD are critical components of cNB for immunoliposomal self-assembly, both warranting further optimization ^{16,48}. In summary, the cNBs make one-step preparation of immunoliposome highly feasible. The shelf life of cNB-LP^{2,000} ensures regulatory compliance, suitability for industrial manufacturing and distribution, and clinical use.

Online content

Any methods, additional references, Nature Portfolio reporting summaries, source data, extended data, supplementary information, acknowledgements, peer review information; details of author contributions and competing interests; and statements of data and code availability are available at https://doi.org/10.1038/s41565-024-01620-6.

References

- Sercombe, L. et al. Advances and challenges of liposome assisted drug delivery. Front. Pharmacol. 6, 286 (2015).
- Liu, Y., Castro Bravo, K. M. & Liu, J. Targeted liposomal drug delivery: a nanoscience and biophysical perspective. *Nanoscale Horiz.* 6, 78–94 (2021).
- 3. Pattni, B. S., Chupin, V. V. & Torchilin, V. P. New developments in liposomal drug delivery. *Chem. Rev.* **115**, 10938–10966 (2015).
- Mitchell, M. J. et al. Engineering precision nanoparticles for drug delivery. Nat. Rev. Drug Discov. 20, 101–124 (2021).
- Mamot, C. et al. Epidermal growth factor receptor-targeted immunoliposomes significantly enhance the efficacy of multiple anticancer drugs in vivo. Cancer Res. 65, 11631–11638 (2005).
- Alavi, M. & Hamidi, M. Passive and active targeting in cancer therapy by liposomes and lipid nanoparticles. *Drug Metab. Pers. Ther.* 34, 20180032 (2019).
- Leserman, L. D., Machy, P. & Barbet, J. Cell-specific drug transfer from liposomes bearing monoclonal antibodies. *Nature* 293, 226–228 (1981).
- Nellis, D. F. et al. Preclinical manufacture of an anti-HER2 scFv-PEG-DSPE, liposome-inserting conjugate. 1. Gram-scale production and purification. *Biotechnol. Prog.* 21, 205–220 (2005).
- Wu, Y. R., Sefah, K., Liu, H. P., Wang, R. W. & Tan, W. H. DNA aptamer-micelle as an efficient detection/delivery vehicle toward cancer cells. *Proc. Natl Acad. Sci. USA* 107, 5–10 (2010).
- Liu, Y. N. et al. EGFR-targeted nanobody functionalized polymeric micelles loaded with mTHPC for selective photodynamic therapy. *Mol. Pharm.* 17, 1276–1292 (2020).
- Hama, S., Sakai, M., Itakura, S., Majima, E. & Kogure, K. Rapid modification of antibodies on the surface of liposomes composed of high-affinity protein A-conjugated phospholipid for selective drug delivery. Biochem Biophys. Rep. 27, 101067 (2021).
- 12. Cho, E. J., Lee, J. W. & Ellington, A. D. Applications of aptamers as sensors. *Annu. Rev. Anal. Chem.* **2**, 241–264 (2009).
- Ma et al. Nucleic acid aptamers in cancer research, diagnosis and therapy. Chem. Soc. Rev. 44, 1240–1256 (2015).
- 14. Li, L. et al. Nucleic acid aptamers for molecular diagnostics and therapeutics: advances and perspectives. *Angew. Chem. Int. Ed. Engl.* **60**, 2221–2231 (2021).
- 15. Muyldermans, S. Nanobodies: natural single-domain antibodies. *Annu. Rev. Biochem.* **82**, 775–797 (2013).
- Chen, X., Zaro, J. L. & Shen, W. C. Fusion protein linkers: property, design and functionality. *Adv. Drug Deliv. Rev.* 65, 1357–1369 (2013).
- 17. Finger, C., Escher, C. & Schneider, D. The single transmembrane domains of human receptor tyrosine kinases encode self-interactions. *Sci. Signal* **2**, ra56 (2009).

- Lāce, I., Cotroneo, E. R., Hesselbarth, N. & Simeth, N. A. Artificial peptides to induce membrane denaturation and disruption and modulate membrane composition and fusion. J. Pept. Sci. 29, e3466 (2023).
- Rahman, M. M., Ueda, M., Hirose, T. & Ito, Y. Spontaneous formation of gating lipid domain in uniform-size peptide vesicles for controlled release. J. Am. Chem. Soc. 140, 17956–17961 (2018).
- Chen, Z., Moon, J. J. & Cheng, W. Quantitation and stability of protein conjugation on liposomes for controlled density of surface epitopes. *Bioconjug. Chem.* 29, 1251–1260 (2018).
- Oliveira, S. et al. Downregulation of EGFR by a novel multivalent nanobody-liposome platform. J. Control. Release 145, 165–175 (2010).
- van der Meel, R. et al. Tumor-targeted nanobullets: anti-EGFR nanobody-liposomes loaded with anti-IGF-1R kinase inhibitor for cancer treatment. J. Control. Release 159, 281–289 (2012).
- 23. Li, N. et al. Surfactant protein-A nanobody-conjugated liposomes loaded with methylprednisolone increase lung-targeting specificity and therapeutic effect for acute lung injury. *Drug Deliv.* **24**, 1770–1781 (2017).
- Khaleghi, S., Rahbarizadeh, F., Ahmadvand, D. & Hosseini, H. R. M. Anti-HER2 VHH targeted magnetoliposome for intelligent magnetic resonance imaging of breast cancer cells. *Cell. Mol. Bioeng.* 10, 263–272 (2017).
- Woll, S. et al. Sortagging of liposomes with a murine CD11b-specific VHH increases in vitro and in vivo targeting specificity of myeloid cells. Eur. J. Pharm. Biopharm. 134, 190–198 (2019).
- Mesquita, B. S. et al. The impact of nanobody density on the targeting efficiency of PEGylated liposomes. *Int. J. Mol. Sci.* 23, 14974 (2022).
- 27. Nishimura, T., Hirose, S., Sasaki, Y. & Akiyoshi, K. Substrate-sorting nanoreactors based on permeable peptide polymer vesicles and hybrid liposomes with synthetic macromolecular channels. *J. Am. Chem.* Soc. **142**, 154–161 (2020).
- Golfetto, O., Hinde, E. & Gratton, E. Laurdan fluorescence lifetime discriminates cholesterol content from changes in fluidity in living cell membranes. *Biophys. J.* 104, 1238–1247 (2013).
- Marsh, D. Thermodynamics of phospholipid self-assembly. Biophys. J. 102, 1079–1087 (2012).
- Hessa, T. et al. Molecular code for transmembrane-helix recognition by the Sec61 translocon. *Nature* 450, 1026–1030 (2007).
- Wan, Y. et al. Velocity effect on aptamer-based circulating tumor cell isolation in microfluidic devices. J. Phys. Chem. B 115, 13891–13896 (2011).
- 32. Grillo, I., Morfin, I. & Prevost, S. Structural characterization of pluronic micelles swollen with perfume molecules. *Langmuir* **34**, 13395–13408 (2018).
- 33. Andersen, T. et al. Chitosan in mucoadhesive drug delivery: focus on local vaginal therapy. *Mar. Drugs* **13**, 222–236 (2015).
- 34. Takikawa, M., Fujisawa, M., Yoshino, K. & Takeoka, S. Intracellular distribution of lipids and encapsulated model drugs from cationic liposomes with different uptake pathways. *Int J. Nanomed.* **15**, 8401–8409 (2020).
- Lin, W. S. & Malmstadt, N. Liposome production and concurrent loading of drug simulants by microfluidic hydrodynamic focusing. *Eur. Biophys. J.* 48, 549–558 (2019).

- Haque, M. E., McIntosh, T. J. & Lentz, B. R. Influence of lipid composition on physical properties and PEG-mediated fusion of curved and uncurved model membrane vesicles: "Nature's own" fusogenic lipid bilayer. *Biochemistry* 40, 4340–4348 (2001).
- Rahman, M. M., Abosheasha, M. A., Ito, Y. & Ueda, M. DNA-induced fusion between lipid domains of peptide-lipid hybrid vesicles. *Chem. Commun.* 58, 11799–11802 (2022).
- Dominguez, L., Foster, L., Straub, J. E. & Thirumalai, D. Impact of membrane lipid composition on the structure and stability of the transmembrane domain of amyloid precursor protein. *Proc. Natl Acad. Sci. USA* 113, E5281–E5287 (2016).
- 39. Wang, B. H. et al. Sequential intercellular delivery nanosystem for enhancing ROS-Induced antitumor therapy. *Nano Lett.* **19**, 3505–3518 (2019).
- Tarafdar, P. K., Chakraborty, H., Dennison, S. M. & Lentz, B. R. Phosphatidylserine inhibits and calcium promotes model membrane fusion. *Biophys. J.* 103, 1880–1889 (2012).
- 41. Lygina, A. S., Meyenberg, K., Jahn, R. & Diederichsen, U. Transmembrane domain peptide/peptide nucleic acid hybrid as a model of a SNARE protein in vesicle fusion. *Angew. Chem. Int Ed.* **50**, 8597–8601 (2011).
- Risselada, H. J., Kutzner, C. & Grubmuller, H. Caught in the act: visualization of SNARE-mediated fusion events in molecular detail. *ChemBioChem* 12, 1049–2011 (2011).
- 43. Kaiser, H. J. et al. Lateral sorting in model membranes by cholesterol-mediated hydrophobic matching. *Proc. Natl Acad. Sci. USA* **108**, 16628–16633 (2011).
- 44. Kozlowska, D. et al. Gadolinium-loaded polychelating amphiphilic polymer as an enhanced MRI contrast agent for human multiple myeloma and non Hodgkin's lymphoma (human Burkitt's lymphoma). RSC Adv. 4, 18007–18016 (2014).
- 45. Ingolfsson, H. I. et al. Lipid organization of the plasma membrane. J. Am. Chem. Soc. **136**, 14554–14559 (2014).
- Scheve, C. S., Gonzales, P. A., Momin, N. & Stachowiak, J. C. Steric pressure between membrane-bound proteins opposes lipid phase separation. J. Am. Chem. Soc. 135, 1185–1188 (2013).
- Schafer, L. V. et al. Lipid packing drives the segregation of transmembrane helices into disordered lipid domains in model membranes. *Proc. Natl Acad. Sci. USA* 108, 1343–1348 (2011).
- 48. Lomize, A. L., Lomize, M. A., Krolicki, S. R. & Pogozheva, I. D. Membranome: a database for proteome-wide analysis of single-pass membrane proteins. *Nucleic Acids Res.* **45**, D250–D255 (2017).

Publisher's note Springer Nature remains neutral with regard to jurisdictional claims in published maps and institutional affiliations.

Springer Nature or its licensor (e.g. a society or other partner) holds exclusive rights to this article under a publishing agreement with the author(s) or other rightsholder(s); author self-archiving of the accepted manuscript version of this article is solely governed by the terms of such publishing agreement and applicable law.

© The Author(s), under exclusive licence to Springer Nature Limited 2024

Methods

The animal experiments were conducted in accordance with the ethical guidelines of the National Institutes of Health. The alpaca experimental protocol was approved by the Institutional Animal Care and Use Committee at RegeneCore Biotech Co., Ltd in Nanjing, China. Mouse experimental protocols were approved by the Institutional Animal Care and Use Committee of the Model Animal Research Center of The Second Hospital of Nanjing, Nanjing University of Chinese Medicine, Nanjing, China. The humane endpoint for mice is 2,000 mm³. The maximal tumour volume observed in this study did not exceed this permitted volume.

Alpaca immunization

A 3-year-old male alpaca (*Vicugna pacos*) was immunized with recombinant extracellular domain of human HER2 (ref. 49). Eight subcutaneous injections were performed at 1-week intervals. Immune sera were collected at the intervals between the fourth and the fifth injection and the third day preceding the last injection. A semi-open shed was used for nighttime housing of alpaca.

NB library construction

Total RNA was extracted from lymphocytes followed by transcription using a SuperScript III kit (ThermoFisher, 18080093). Complementary DNA was amplified to get NB coding sequences^{49,50}. Purified polymerase chain reaction (PCR) products were digested with restriction enzymes and ligated with phagemid. Recombinant phagemids were transformed with TG1 cells by electroporation^{49–54}. The transformants were plated on Luria Broth broth solid medium supplied with ampicillin sodium.

Screening, expression and purification of NB

The obtained library was screened by phage display. Three rounds of bio-panning were carried out, and 282 colonies were selected to perform enzyme-linked immunosorbent assay. Positive colonies were sequenced. Eventually, the candidate NB were expressed by CHO cells followed by purification⁴⁹.

Antibody-dependent cell cytotoxicity

Herceptin, human IgG isotype control and NB at 15 μ g ml $^{-1}$ with fivefold serial dilutions were incubated with 2×10^5 SK-BR-3 cells for 30 min. Peripheral blood mononuclear cells were further added and incubated at 37 °C for 15 h. Approximately 50 μ l of supernatant from each well was collected and mixed with 50 μ l of lactate dehydrogenase reagent. OD₄₉₂ and OD₆₅₀ were measured.

NB affinity measurement

The binding kinetics of NB to HER2 were determined using Octet RED 96e system (FortéBio, v11.0). All experiments were performed at 30 °C, and reagents were prepared in 0.1% bovine serum albumin, 0.02% Tween20 PBS, pH 7.4 buffer. NB was immobilized onto biosensors followed by association and dissociation measurements with human HER2 for a time window of 70 s and 30 s, respectively.

Capillary isoelectric focusing

The isoelectric point of NBs and cNBs was determined with Maurice analyser (iCE 4.0.0). The column was filled with samples followed by applying 1.5 kV DC to pre-focus for 1 min and 3 kV direct current for 7 min. The electropherogram along with the signal were recorded. Exposure time was optimized at 3 s.

NB induced SK-BR-3 cell proliferation inhibition assay

Herceptin, human IgG isotype and NB at $15 \,\mu g \,ml^{-1}$ with fivefold serial dilutions were incubated with 10,000 SK-BR-3 cells for $48 \,h$. Cell viability was measured followed by calculation of EC₅₀.

Molecular modelling analysis

The structure of NB, HER2, NB/HER2 complex and cNB was predicted with AlphaFold multimer (v2.3.0). GROMACS (v2021.03) was used to investigate the conformation of NB/HER2 complex s4. The force field amber14sb was used to parameterize proteins 55. The TIP3P was used for the waters 56. This NB/HER2 complex was solvated in a water box, and then the system was neutralized. The energy of the system was minimized. The position of heavy atoms was restricted to run constant volume equilibration and constant pressure equilibration at 300 K and 1 bar. Upon completion of the equilibration phases, a 200-ns unrestrained simulation was performed. The energy and trajectory were recorded every 20 ps. ChimeraX (v1.6.1) and Pymol (v2.5.7) were used to map interaction patterns and animate kinetic trajectories 57,58. Similarly, the cNB self-assembly was assessed 59,60.

cNB production with E. coli

dE.coli BL21 Star (DE3) competent cells were transformed with recombinant plasmid ordered from GenScript. Cultures were incubated in 37 °C for 4 h and 15 °C for 16 h, respectively. Once cell density reached to an OD of 0.6–0.8 at 600 nm, 0.5 mM isopropyl β -D-1-thiogalactopyranoside was introduced. cNBs were collected and characterized by sodium dodecyl sulfate–polyacrylamide gel electrophoresis and western blot.

Preparation of liposomes and cNB-LP

DMPC, DOPE and cholesterol at molar ratios of 700:200:100 were used to prepare liposomes. The organic solvent was evaporated using argon. Subsequently, the lipid film containing tube was placed under vacuum overnight. The lipid film was hydrated at 40 °C for 5 min. Meanwhile, cNB solution or PBS was introduced. The mixture was sonicated followed by stirring at 40 °C overnight. An Avanti Mini-Extruder equipped with a 0.1- μ m polycarbonate membrane was used to prepare 100-nm LPs and cNB-LPs. Free cNBs were removed using a 100 kDa membrane filter.

Fluorescence microscope

cNB-LPs were stained with anti-His tag antibodies (Santa Cruz, sc-8036 AF488, 1:500; GenScript A01800, 1:500) at 4 °C. Surplus antibodies were removed with a centrifugal filter. The antibody-labelled cNB-LPs were resuspended in PBS. In cell binding assay, -5×10^5 of cNB-LP⁵⁰⁰ and cNB-LP^{1,000} were incubated with 5×10^3 cells for 30 min at 37 °C, and unbound cNB-LPs were removed. Fluorescence images were acquired with Olympus IX83 (v01.04.07) and Leica SP5 (v2.0.2).

Transmission electron microscope

Approximately $5\,\mu$ l of sample was placed on a 400-mesh grid and negatively stained. For cryo-TEM, $5\,\mu$ l of sample was added to a 200-mesh grid, blotted with FEI Vitrobot before plunging into liquid ethane, and transferred to a cryo-sample holder. Samples were examined in a FEI Tecnai TEM.

cNB anchor efficiency

Micro-bicinchoninic acid protein assay (ThermoFisher, 23235) was used to determine anchor efficiency. Various cNB-LPs were prepared as described. Free cNBs were separated twice using centrifugal filters. The concentration of free cNB was measured followed by calculation of anchor efficiency.

FRET

FRET was measured with TECAN Spark (SparkControl v1.2 SP1). To prepare cNB-LPs, 1,000 μ M lipid mix:10 μ M NBD-PE:10 μ M Rhod-PE were mixed in a glass tube to make a thin film. Subsequently, 0.015 and 0.054 μ M cNB were added to prepare 1 ml of cNB-LP 500 and cNB-LP 4000 . Similarly, 1,000.015 μ M (or 1,000.054 μ M) lipid mix:10 μ M NBD-PE:10 μ M Rhod-PE were mixed to prepare plain LPs as negative controls. In another experiment, purified cNB-LP 500 and cNB-LP 1,000

were incubated with both anti-His6 tag antibody (Santa Cruz, sc-8036 AF488 and AF546, 1:500). Respective donor-labelled vesicles were used to calculate the FRET efficiency in the absence and presence of the acceptor according to $E(\%) = (ID - IDA)/(ID) \times 100$, where ID and IDA are the donor intensities of samples containing only donor-labelled vesicles and samples with both donor- and acceptor-labelled vesicles, respectively.

Laurdan assay

The membrane fluidity was measured with a Laurdan assay. A general polarization value, GP_{340} , was calculated as $GP_{340} = (I_{440} - I_{490})/(I_{440} + I_{490})$, where I_{440} and I_{490} are emission intensities at 440 and 490 nm. The temperature ranged from 10 °C to 42 °C.

Differential scanning calorimetry

Desired concentrations of $50\,\mu$ l of cNB-LPs, LPs and cNBs were placed on aluminium pans and analysed with TA Instrument Q200 (TRIOS 5.1.1). The temperature ranged from $10\,^{\circ}$ C to $60\,^{\circ}$ C with a heating rate of $10\,^{\circ}$ C min⁻¹.

Circular dichroism

Circular dichroism data were obtained using a JASCO J-1500 (Spectra Manager II, v2.8) equipped with a 1-cm optical path length cell at 25 $^{\circ}$ C. Approximately 0.01 mM cNBs, LPs and cNB-LP^{2,000} in PBS were measured, respectively.

Atomic force microscopy

Samples were deposited on the mica surface. Scanning was performed using a Bruker Dimension Icon AFM (AutoMET) in contact mode with a scan rate of 1 Hz, resolution of 512 \times 512 pixels, scanning angle of 0 and a set point below 0.1 nN (ref. 61). The force curve was obtained by indenting centrally an attached vesicle with a maximum force of 1.5 nN and a rate of 0.145 $\mu m \, s^{-1}$. The Young's modulus was extracted using PeakForce Quantitative Nanomechanical Mapping 62 .

SAXS

The SAXS data were acquired with the Rigaku BioSAXS2000 $^{\rm nano}$. The cNBs, LPs and cNB-LP $^{\rm 2,000}$ in PBS were loaded into a quartz flow-cell mounted on a stage maintained at 4 $^{\rm o}$ C, aligned with the X-ray beam, respectively. A series of three 10-min scattering images were collected. The collected data were processed using the Rigaku SAXSLab. Solvent envelopes were computed through DENSS $^{\rm 63}$.

Calculation of membrane stiffness

We used 2D model of lipid bilayer with inserted cNB (Supplementary Fig. 12a,b). The outer radius and the thickness of the liposome are R and h, respectively. The inner radius of the liposome was used to establish a relation between N_p (the number of lipids) and N_p (the number of cNB). The areal packing density of the lipids was $\rho = \pi/(2\sqrt{3})$ (Supplementary Fig. 12c)⁶⁴, where r_p is the radius of the lipid head. The total inner surface area of the liposome is $\rho A = N_p A_p + N_n A_n$, where $A = 4\pi (R - h)^2$, $A_p = \pi r_p^2$, $A_n = \pi r_n^2$ and r_n is the radius of a cNB. This equation calculates N_p . The number of lipids surrounding a lipid is $n_p = 6$, whereas the average number of lipids surrounding a cNB is $n_{\rm n}=\pi/\arcsin\left(\frac{r_{\rm p}}{(r_{\rm p}+r_{\rm n})}\right)$ (Supplementary Fig. 12d). We approximated the force interaction between two adjacent lipids by a spring of constant $k_{\rm p}$ (Supplementary Fig. 12e). These springs around a molecule were in parallel under the membrane tension. Therefore, the effective stiffness due to lipid–lipid interaction was $n_p k_p$. Similarly, the effective stiffness due to cNB-lipid interaction was $n_n k_n$, where k_n is the spring constant between a cNB and a lipid molecule (Supplementary Fig. 12f). The effective stiffness of the membrane is $k = [(n_p k_p)(N_p A_p)]$ $+(n_nk_n)(N_nA_n)]/(N_pA_p+N_nA_n)$. In the absence of cNB, the membrane stiffness is $k_0 = n_p k_p$. We normalized the effective stiffness of the membrane by k_0 and obtained a relative stiffness $k_r = k/k_0$. If $k_r > 1$, the effective stiffness of the membrane increased with added cNB. Otherwise, adding cNB would reduce the membrane stiffness. Structure stability required $N_{\rm n}/N_{\rm p}\ll 1$, that is, $N_{\rm n}\ll 4\rho/\left(1+\left(\frac{r_{\rm n}}{r_{\rm p}}\right)^2\right)\left((R-h)/r_{\rm p}\right)^2$. The typical geometrical parameter of $r_{\rm p}, r_{\rm n}, h$ and R are 0.45 nm, 0.6 nm,

5 nm and 50 nm, respectively. With these parameters, the structure stability condition required $N_n \ll 13,000$. The number of cNB used in the experiments satisfied this condition. The model prediction of the effective membrane stiffness as a function of the number of cNB was plotted for different ratios of $\kappa = k_n/k_p$ (Supplementary Fig. 12g). For the NBs to enhance the stiffness of the membrane, $\kappa > 0.89$ should be satisfied. We next estimated the ratio κ . A generic repulsion-attraction model was used for the intermolecular interactions (Supplementary Fig. 12h). The bonding energy was $E = -A_1 r^{-\alpha_1} + A_2 r^{-\alpha_2}$, where r is the intermolecular distance, $\alpha_2 > \alpha_1 > 0$ and $A_1 > A_2 > 0$. α_1 and α_2 reflect the nature of the bonding energy. We assumed these two values were the same for lipid-lipid interaction and cNB-lipid interaction. However, A_1 and A_2 are molecule specific. At the equilibrium distance $r = r_0$, the minimum energy is E_0 . The bonding force is F = dE/dr. The effective spring constant k is proportional to the slope of the bonding force, that is, $k \propto \mathrm{d}F/\mathrm{d}r|_{r=r_0} = -\left[(\alpha_1\alpha_2)/r_0^2\right]E_0$. Therefore, $\kappa = \left(E_{0,\mathrm{n}}/E_{0,\mathrm{p}}\right)\left(r_{0,\mathrm{p}}^2/r_{0,\mathrm{n}}^2\right)$. In our problem, $r_{0,n} \approx r_{0,p}$ and $E_{0,n}/E_{0,p} \approx 1.15$. Then $\kappa \approx 1.15$, indicating that adding cNB increased the effective stiffness of the liposome membrane (Supplementary Fig. 12g).

Computational model of interaction between cNB-LP and HER2-expression cells

A 20-um cancer cell and a 100-nm cNB-LP were used for computation. The probability of bond formation between NB and HER2 were modelled using a probabilistic kinetic formulation⁶⁵⁻⁶⁷. The probability of cNB-LP adhesion, denoted as P_a , was estimated by $P_{\rm a}=m_{\rm r}m_{\rm l}K_{\rm a}^{0}A_{\rm c}\exp\left[-\frac{M}{k_{\rm B}T}\right]$, where $m_{\rm l}$ and $m_{\rm r}$ represent the ligand and receptor density, respectively, K_a^0 refers to the association constant at zero load of the cNB-HER2 pair, while A_c is the contact area between cNB-LP and cancer cell surfaces, f is the force per ligand-receptor pair, and λ is the characteristic length of the ligand receptor (assumed to be 0.1 nm), $k_B T$ is the thermal energy. The drag force F and torque Tinduced by the fluid were balanced by the force produced by the ligand receptor pairs. When the LP is in point contact with the surface in a flow with a shear rate of $\dot{\gamma}$, the force and torque are approximated as $F \approx 10\pi r^2 \mu \dot{\gamma}$ and $T \approx 12\pi r^3 \mu \dot{\gamma}$, respectively⁶⁸, where *r* is the radius of the cNB-LP and μ is the fluid viscosity. Assuming that the force F is distributed uniformly among all the NB-HER2 bonds, and the torque Twas shared uniformly only among the stretching bonds, the force per ligand-receptor pair was calculated as $f = \frac{1}{m_r} \left[\frac{F}{A_c} + \frac{2T}{A_c r_c} \right]$, where r_c is the radius of contact area. Data were plotted with MATLAB (R2022a).

Zeta potential measurement

Zeta potential measurement was conducted using a Zetasizer Nano (v3.30). Approximately 10 μ l of the sample in 990 μ l of de-ionized water was transferred to a Malvern Clear Zeta Potential cell. Three independent aliquots were analysed three times.

Nanosight measurement

LPs and cNB-LP^{2,000} in 200 μ l of PBS were measured with Nanosight NS300 (v3.00).

Drug loading and release profiling

The amount of loaded 5FU in LPs and cNB-LP^{2,000} was measured by high-performance liquid chromatography (Waters Acquity v1.51). Loading efficiency was calculated by $\frac{\text{total-unloaded}}{\text{total}} \times 100\%$. To measure

5FU release, samples were placed in a 300 kDa dialysis membrane

(Spectrum Labs). Samples were taken at various timepoints and analysed. Similarly, the respective loading efficiency and release profiles of dextran-3k (Krackeler, 45-DF4) and dextran-10k (Krackeler, 45-FD10S) were determined.

Cell culture

Cells were ordered from ATCC. The SK-BR-3 (HTB-30), MDA-MB-231 (HTB-26), T24 (HTB-4), HT-29 (HTB-38), LS-174T (CL-188), NCI-N87 (CRL-5822), NCI-H838 (CRL-5844) and NCI-H2170 cells (CRL-5928) were maintained in Dulbecco's modified Eagle medium supplied with 10% foetal bovine serum (FBS). SNU-5 (CRL-5973) and RT4 cells (HTB-2) were cultured in Iscove's modified Dulbecco's medium and McCoy's 5A medium supplied with 10% FBS.

Western blot

Samples were electrotransferred onto a nitrocellulose membrane. The membrane was blocked with non-fat milk in PBS/0.05% Tween20 for 30 min and washed thrice with DI water. Samples were incubated overnight at 4 °C with horseradish peroxidase-labelled antibodies against His6 tag (Santa Cruz, sc-8036, 1:500), HER2 (Santa Cruz, sc-08, 1:500) and GAPDH (Santa Cruz, sc-32233, 1:500). Samples were washed with PBS/0.05% Tween20 for 10 min thrice before imaging.

CCK-8 assay

5FU loaded LPs and cNB-LP 2,000 in a series of concentrations were incubated with 4,000 SK-BR-3 cells. Five replicates were made for each measurement. Cells were cultured for 24 h at 37 °C followed by incubated with 10 μ l of CCK-8 for 2 h. The absorbance at 450 nm was measured.

Colony formation assay

Approximately 500 SK-BR-3 cells were seeded into a well in a six-well plate in triplicate, treated with PBS, 5FU, NB, 5FU-loaded LPs and 5FU-loaded cNB-LP^{2,000} for 2 weeks until visible clones were formed. The formed clones were rinsed with PBS thrice followed by numeration.

Invasion assay

A 24-well Transwell chamber with a pore size of 8 μ m was used. Each insert was coated with 50 μ l of Matrigel (1:3 dilution, Corning, 354234). Approximately 1×10^4 SK-BR-3 cells in 300 μ l of medium were transferred to the upper Matrigel chamber and incubated for 48 h. Medium supplemented with 15% FBS was used as a chemoattractant and added to the lower chamber. Cells that passed through the filter were counted.

SK-BR-3 spheroid assay

Round-bottom Cellstar Cell-Repellent Surface plates were used. Approximately 1×10^4 SK-BR-3 cells in $100~\mu l$ of culture medium containing 3.5% Matrigel was added to wells. When diameter reached -100 μm , spheroids were treated with PBS, 5FU, NB, 5FU-loaded LPs and 5FU-loaded cNB-LP^{2,000} for 7 days. The spheroid volume were measured.

Blood tests

Five BALB/c mice ($^{-1}$ 8–22 g, 6 weeks) were intravenously administrated with 5 mg kg $^{-1}$ NB for four doses. Approximately 250 μ l of peripheral blood was collected and analysed with Mindray BC-6200 and Beckman Coulter AU480 (v1.72).

Animal models

Approximately 2×10^6 SK-BR-3 cells were inoculated to the mammary pad of BALB/c mice (-18–22 g, 6 weeks). The housing conditions for the mice were as follows: 12:12 h dark/light cycle, ambient temperature of $22\pm1\,^{\circ}$ C, and -55% of humidity. Tumours were allowed to grow to a size of -100 mm³. The mice were then randomly divided into five groups. Drug was intravenously administrated every 2–3 days (20 mg of 5FU-equivalent per kilogram of body weight per dose) for 4 weeks. Mice were killed to collect tumours. To study pharmacokinetics and biodistribution of 5FU,

0.1–0.3 g tissue samples were collected at 24-h post-administration followed by high-performance liquid chromatography analysis. In parallel, 2×10^6 NCI-N87 cells were subcutaneously inoculated to the flanks of BALB/c mice (-18–22 g, 6 weeks). Drug was intravenously administered every 2–3 days (50 mg of 5FU-equivalent per kilogram of body weight per dose) for 4 weeks. Moreover, SK-BR-3 orthotropic models were used to study the overall survival of mice. Fifty female BALB/c mice (-18–22 g, 6 weeks) were randomly divided into five groups and intravenously injected with 20 mg of 5FU-equivalent per kilogram of body weight per dose. Tumour growth, physical wellbeing and survival were monitored up to 90 days. At day 90, surviving mice were killed.

Statistical analysis

Quantitative results were presented as mean \pm standard deviation (s.d.). Student's unpaired t-test was used to compare control treated samples against experimental samples. For multiple treated groups, statistical significance was examined using one-way analysis of variance (ANOVA). The sample size was not calculated before experiments. It was determined by the number of biological replicates necessary for ensuring statistical significance. Data collection and analysis were not performed blind to the conditions of the experiments. No animals for data points were excluded from the analysis.

Reporting summary

Further information on research design is available in the Nature Portfolio Reporting Summary linked to this article.

Data availability

The authors declare that all data supporting the findings of this study are available within the paper and Supplementary Information files. Additional information and unique biological materials can be requested from the corresponding author upon reasonable request. Custom code was not involved in this study.

References

- 49. Pardon, E. et al. A general protocol for the generation of nanobodies for structural biology. *Nat. Protoc.* **9**, 674–693 (2014).
- 50. Jovcevska, I. et al. TRIM28 and β-actin identified via nanobody-based reverse proteomics approach as possible human glioblastoma biomarkers. *PLoS ONE* **9**, e113688 (2014).
- 51. Hmila, I. et al. A bispecific nanobody to provide full protection against lethal scorpion envenoming. FASEB J. 24, 3479–3489 (2010).
- 52. Farajpour, Z., Rahbarizadeh, F., Kazemi, B. & Ahmadvand, D. A nanobody directed to a functional epitope on VEGF, as a novel strategy for cancer treatment. *Biochem. Biophys. Res. Commun.* **446**, 132–136 (2014).
- 53. Roovers, R. C. et al. A biparatopic anti-EGFR nanobody efficiently inhibits solid tumour growth. *Int. J. Cancer* **129**, 2013–2024 (2011).
- 54. Abraham, M. J. et al. GROMACS: high performance molecular simulations through multi-level parallelism from laptops to supercomputers. *SoftwareX* **1-2**, 19–25 (2015).
- Nguyen, H., Maier, J., Huang, H., Perrone, V. & Simmerling, C. Folding simulations for proteins with diverse topologies are accessible in days with a physics-based force field and implicit solvent. J. Am. Chem. Soc. 136, 13959–13962 (2014).
- Jorgensen, W. L., Chandrasekhar, J., Madura, J. D., Impey, R.
 W. & Klein, M. L. Comparison of simple potential functions for simulating liquid water. J. Chem. Phys. 79, 926–935 (1983).
- 57. Goddard, T. D. et al. UCSF ChimeraX: meeting modern challenges in visualization and analysis. *Protein Sci.* **27**, 14–25 (2018).
- 58. DeLano W. L. PyMOL molecular viewer: updates and refinements. *Abstr. Pap. Am. Chem. S* **238**, (2009).
- 59. Genheden, S. & Ryde, U. The MM/PBSA and MM/GBSA methods to estimate ligand-binding affinities. *Expert Opin. Drug Discov.* **10**, 449–461 (2015).

- Valdes-Tresanco, M. S., Valdes-Tresanco, M. E., Valiente, P. A. & Moreno, E. gmx_MMPBSA: a new tool to perform end-state free energy calculations with GROMACS. J. Chem. Theory Comput. 17, 6281–6291 (2021).
- 61. Et-Thakafy, O. et al. Mechanical properties of membranes composed of gel-phase or fluid-phase phospholipids probed on liposomes by atomic force spectroscopy. *Langmuir* **33**, 5117–5126 (2017).
- Dokukin, M. E. & Sokolov, I. Quantitative mapping of the elastic modulus of soft materials with HarmoniX and PeakForce QNM AFM modes. *Langmuir* 28, 16060–16071 (2012).
- 63. Custodio, T. F. et al. Selection, biophysical and structural analysis of synthetic nanobodies that effectively neutralize SARS-CoV-2. *Nat. Commun.* **11**, 5588 (2020).
- 64. Callister, W. D. & Rethwisch, D. G. Materials Science and Engineering: An Introduction Vol. 7 (Wiley, 2020).
- McQuarrie, D. A., Jachimowski, C. & Russell, M. Kinetics of small systems. II. J. Chem. Phys. 40, 2914–2921 (1964).
- Decuzzi, P. & Ferrari, M. The adhesive strength of non-spherical particles mediated by specific interactions. *Biomaterials* 27, 5307–5314 (2006).
- Piper, J. W., Swerlick, R. A. & Zhu, C. Determining force dependence of two-dimensional receptor-ligand binding affinity by centrifugation. *Biophys. J.* 74, 492–513 (1998).
- 68. Goldman, A. J., Cox, R. G. & Brenner, H. Slow viscous motion of a sphere parallel to a plane wall 0.2. Couette flow. *Chem. Eng. Sci.* **22**, 637–651 (1967).

Acknowledgements

Y.W. thanks the support from National Cancer Institute R01CA230339 and R37CA255948. Y.L. is supported by NSF 2303648. The opinions, findings, conclusions or recommendations expressed are those of the

authors and do not necessarily reflect the views of any of the funding agencies. L.W. thanks the support from Jiangsu Provincial Medical Youth Talent QNRC2016054 and the Leading-Edge Technology Program of Jiangsu Natural Science Foundation BK20212012. S.H.C. thanks the support from office of the Direct, National Institutes of Health S100D026822-01.

Author contributions

The project was designed by Y.W., Lixue W. and L.P.L. M.R., J.W., G.W., Z.S., Y.L., Y.C., J.M., Y.Y., Lefei W., S.W., J.T., J.L., T.Z., C.Z. and S.H.C. performed the experiments, collected and analysed the data. All authors contributed to the writing of the paper, discussed the results and implications, and edited the paper at all stages.

Competing interests

The authors declare no competing interests.

Additional information

Supplementary information The online version contains supplementary material available at https://doi.org/10.1038/s41565-024-01620-6.

Correspondence and requests for materials should be addressed to Lixue Wang, Luke P. Lee or Yuan Wan.

Peer review information *Nature Nanotechnology* thanks Bruno Fonseca-Santos Ali Makky and the other, anonymous, reviewer(s) for their contribution to the peer review of this work.

Reprints and permissions information is available at www.nature.com/reprints.

nature portfolio

Corresponding author(s):	Yuan Wan
Last updated by author(s):	Dec 21, 2023

Reporting Summary

Nature Portfolio wishes to improve the reproducibility of the work that we publish. This form provides structure for consistency and transparency in reporting. For further information on Nature Portfolio policies, see our <u>Editorial Policies</u> and the <u>Editorial Policy Checklist</u>.

For all statistical analyses, confirm that the following items are present in the figure legend, table legend, main text, or Methods section

~					
< ⋅	トつ	+1	ıst	11.	\sim
٠,			151	-14	, n

n/a	Confirmed
	The exact sample size (n) for each experimental group/condition, given as a discrete number and unit of measurement
	A statement on whether measurements were taken from distinct samples or whether the same sample was measured repeatedly
	The statistical test(s) used AND whether they are one- or two-sided Only common tests should be described solely by name; describe more complex techniques in the Methods section.
	A description of all covariates tested
\boxtimes	A description of any assumptions or corrections, such as tests of normality and adjustment for multiple comparisons
	A full description of the statistical parameters including central tendency (e.g. means) or other basic estimates (e.g. regression coefficient) AND variation (e.g. standard deviation) or associated estimates of uncertainty (e.g. confidence intervals)
\boxtimes	For null hypothesis testing, the test statistic (e.g. <i>F</i> , <i>t</i> , <i>r</i>) with confidence intervals, effect sizes, degrees of freedom and <i>P</i> value noted <i>Give P values as exact values whenever suitable.</i>
\boxtimes	For Bayesian analysis, information on the choice of priors and Markov chain Monte Carlo settings
\boxtimes	For hierarchical and complex designs, identification of the appropriate level for tests and full reporting of outcomes
X	Estimates of effect sizes (e.g. Cohen's <i>d</i> , Pearson's <i>r</i>), indicating how they were calculated
	Our web collection on <u>statistics for biologists</u> contains articles on many of the points above.

Software and code

Policy information about availability of computer code

Data collection

Tecan Spark plate reader (SparkControl v1.2 SP1), Octet RED96e system (v 11.0), Maurice analyzer (iCE 4.0.0), AlphaFold multimer (v2.3.0), GROMACS (2021.03), ChimeraX (v1.6.1), Pymol (v2.5.7), Olympus IX83 (v01.04.07), Leica SP5 (Leica Lite 2.0.2), Bruker Dimension Icon AFM (AutoMET), JASCO J-1500 (Spectra Manager II (v2.8), TA Instruments Q200 (TRIOS 5.1.1), Zetasizer Nano ZS (v3.30), Nanosight NS300 (v3.00), MATLAB (R2022a), Waters Acquity (v1.51), Beckman Coulter AU480 (v1.72)

Data analysis

Tecan Spark Magellan (3.x), Originpro 2023 (10.0)

For manuscripts utilizing custom algorithms or software that are central to the research but not yet described in published literature, software must be made available to editors and reviewers. We strongly encourage code deposition in a community repository (e.g. GitHub). See the Nature Portfolio guidelines for submitting code & software for further information.

Data

Policy information about availability of data

All manuscripts must include a <u>data availability statement</u>. This statement should provide the following information, where applicable:

- Accession codes, unique identifiers, or web links for publicly available datasets
- A description of any restrictions on data availability
- For clinical datasets or third party data, please ensure that the statement adheres to our <u>policy</u>

The authors declare that all data supporting the findings of this study are available within the paper and Supplementary Information files. Source data is provided with this paper. Additional information and unique biological materials can be requested from the corresponding author upon reasonable request.

Human research participants

Reporting on sex and gender	n.a.
Population characteristics	n.a.

Recruitment n.a.

Note that full information on the approval of the study protocol must also be provided in the manuscript.

Policy information about studies involving human research participants and Sex and Gender in Research.

Field-specific reporting

Fthics oversight

Sample size

Please select the one below	v that is the best fit for your research. If	you are not su	ure, read the appropriate sections before making your	selection.
X Life sciences	Behavioural & social sciences	Ecological	, evolutionary & environmental sciences	

For a reference copy of the document with all sections, see <u>nature.com/documents/nr-reporting-summary-flat.pdf</u>

Life sciences study design

All studies must disclose on these points even when the disclosure is negative.

n.a

in studies must disclose on these points even when the disclosure is negative.

The sample size was not calculated before experiments. But at least five biological replicates were used to satisfy t-test or ANOVA test. To get more reliable results and statistical significance, >10 replicates were used in few assays. In brief, the sample size is determined by the number of biological replicates necessary for ensuring statistical significance.

Data exclusions No data were excluded from the analyses

Replication 3-10 times, depending on the number of treatments, availability of material, experimental unit, and expenses. All attempts at replication were successful.

Randomization Mice were then randomly divided into groups. Fluorescence images were randomly taken from substrates. Random sampling was strictly executed in whole study.

Blinding n.a.; not involved. The operator must know which were the experimental groups.

Reporting for specific materials, systems and methods

We require information from authors about some types of materials, experimental systems and methods used in many studies. Here, indicate whether each material, system or method listed is relevant to your study. If you are not sure if a list item applies to your research, read the appropriate section before selecting a response.

Materials & experime	ental sy	stems Methods	
n/a Involved in the study		n/a Involved in the study	
Antibodies		ChIP-seq	
Eukaryotic cell line:	S	Flow cytometry	
Palaeontology and	archaeolo	pgy MRI-based neuroimaging	
Animals and other	organism:		
Clinical data			
Dual use research of	of concerr		
Antibodies			
Antibodies used			
Validation	The specificity of the antibodies employed in this study were validated by immunoblot analysis. Appropriate positive and negative controls were included in every experiment. To check for antibody specificity, we used knockout cell lines (for protein of interest) as a control and ensure the right size bands disappear in those cells. In addition, we monitored the Antibody Registry database (http://antibodyregistry.org/). Additional validation files can be found through vendors' online Datasheet. Herceptin (https://assets.roche.com/f/170883/x/7baaae39a7/herceptin-iv-sc-pi-feb-2021.pdf), human IgG isotype (https://bioxcell.com/pub/media/tds/BE0092-TDS.pdf), anti-His GenScript (https://www.genscript.com/product/documents?cat_no=A01800&catalogtype=Document-COA), anti-His Santa Cruz (https://datasheets.scbt.com/sc-8036.pdf), anti-HER2 (https://datasheets.scbt.com/sc-08.pdf), anti-GAPDH (https://datasheets.scbt.com/sc-32233.pdf)		
Eukaryotic cell lir Policy information about <u>c</u> Cell line source(s)		and Sex and Gender in Research SK-BR-3, MDA-MB-231, T24, RT4, HT-29, LS-174T, SNU-5, NCI-N87, NCI-H838, and NCI-H2170 (ATCC); dE. coli BL21 star	
Authentication All cell lines were au		All cell lines were authenticated using the short tandem repeat (STR) profiling (Genetica).	
, ' '		All cell lines were periodically tested for mycoplasma contamination using e-Myco Plus kit (iNtRON Biotechnology). None of the cell lines were contaminated.	
Commonly misidentified lines (See ICLAC register)		no commonly misidentified cell lines were used in this study.	
Animals and othe	er rese	earch organisms	
Policy information about <u>s</u> Research	tudies in	volving animals; ARRIVE guidelines recommended for reporting animal research, and Sex and Gender in	
Laboratory animals	boratory animals A male Alpaca (Vicugna pacos), ~3-year old; A semi-open shed was used for nighttime housing of alpaca. BALB/c mice, ~18-22 g, 6 weeks; The housing conditions for the mice were as follows: 12:12 h dark/light cycle, ambient temperature of 22±1 °C, and ~55% of humidity		
Wild animals	no wild	no wild animals were used in the study.	
Reporting on sex	Either male or female alpaca can be used for generation nanobodies. In this study RegeneCore Biotech Co. Ltd used a male alpaca. HER2 overexpression across a broad spectrum of tumor types, and our findings apply to both male and female sex. Breast cancer cell line SK-BR-3 cells were inoculated to the mammary pad of mice to develop orthotopic xenograft tumor models. Therefore, female mice were used for the in vivo experiments. Gastric Carcinoma cell line NCI-N87 cells were subcutaneously inoculated to the flanks of mice to develop xenograft tumor models. Therefore, both male and female mice were used for the in vivo experiments.		

Ethics oversight The animal experiments were conducted in accordance with the ethical guidelines of the National Institutes of Health. The alpaca experiment protocol involving immunization, collection of blood samples, and construction of VHH library was approved by the Institutional Animal Care and Use Committee (IACUC) at RegeneCore Biotech Co., Ltd in Nanjing, China

Mouse experiments were approved by and performed by guidelines from the Institutional Animal Care and Use Committee (IACUC)

of the Model Animal Research Center of the Second Hospital of Nanjing.

Note that full information on the approval of the study protocol must also be provided in the manuscript.

no field collected samples were used in the study.

Field-collected samples